Title

Quantitative comparisons of contrast in experimental and simulated bright-field scanning transmission electron microscopy images

Journal

Physical Review B, 80

Author

Stemmer, Susanne

Publication Date

2009

DOI

10.1103/PhysRevB.80.174106

Peer reviewed

Quantitative comparisons of contrast in experimental and simulated bright-field scanning transmission electron microscopy images

James M. LeBeau,[1] Adrian J. D'Alfonso,[2] Scott D. Findlay,[3]

Susanne Stemmer,[1] Leslie J. Allen[2]

[1]Materials Department, University of California, Santa Barbara, CA 93106-5050, U.S.A.

[2]School of Physics, University of Melbourne, Victoria 3010, Australia

[3]Institute of Engineering Innovation, School of Engineering, The University of Tokyo, Tokyo, 113-8656, Japan

Abstract

Quantitative, atomic resolution bright-field scanning transmission electron microscopy experiments are reported. The image intensities are placed on an absolute scale relative to the incident beam intensity. Features in the experimental images, such as contrast reversals, intensities and the image contrast, are compared with image simulations that account for elastic scattering and the effect of phonon scattering. Simulations are carried out using both the multislice absorptive and frozen phonon simulation methods. For a $SrTiO_3$ sample with thicknesses between 4 and 25 nm, both models agree within the experimental uncertainty. We demonstrate excellent agreement between the simulated and the experimentally observed image contrast. The implications for the contrast mismatch commonly reported for high-resolution transmission electron microscopy using plane-wave illumination are discussed.

I. Introduction

High-resolution transmission electron microscopy (HRTEM) and scanning transmission electron microscopy (STEM) are two of the most powerful techniques capable of investigating local atomic arrangements. While STEM uses a finely focused probe and HRTEM uses plane wave illumination conditions, interpretation of images in both techniques critically relies on image simulations [1]. For example, the intensity of columns in high-angle annular dark-field (HAADF or Z-contrast) imaging in STEM is sensitive to thermal diffuse scattering (TDS) and Debye-Waller factors. Phase contrast and associated contrast reversals dominate the appearance of HRTEM images. Quantitative agreement, to within a few percent, has recently been shown between experiments and theory in Z-contrast STEM [2, 3]. These results show that current understanding of image formation is adequate; in particular models correctly account for the contributions of TDS, which dominates Z-contrast images. In contrast, quantitative comparisons in HRTEM have often been plagued by a large (100 - 400%) discrepancy between theory and experiment, which has become known as the Stobbs factor [4-8]. Recently, it has been shown that careful consideration of the image recording process may account for the Stobbs factor in HRTEM [9, 10].

Bright-field STEM, in which lattice images are formed by interference of overlapping convergent beam discs [11], is related to HRTEM via the principle of reciprocity [12]. Similar to HRTEM, these images are dominated by phase contrast [12]. Bright-field STEM images can be acquired along with Z-contrast images without the need to change the electron optical conditions of the microscope (except for slight adjustments in the defocus), providing near-simultaneous complementary information. For example, similar to HRTEM [13], bright

field STEM images are more sensitive than Z-contrast images to light columns such as oxygen [14].

In this paper, we report on quantitative comparisons between experiments and theory in bright-field STEM. Experimental bright-field STEM images are placed on an absolute scale, using a previously developed method [15], so that they can be directly compared with image simulations. We demonstrate near perfect agreement between simulations and experiment and discuss the implications for HRTEM.

II. Experimental

A $SrTiO_3$ single crystal was thinned to electron transparency by wedge-polishing and Ar-ion milling for observation along [100]. A field emission electron microscope (FEI Titan 80-300) with a super-twin lens (C_s ~ 1.2 mm) operated at 300 kV was used for bright-field STEM, position averaged convergent beam electron diffraction (PACBED) and Z-contrast imaging. The probe convergence semi-angle was 9.4 mrad. The microscope was aligned using a Ronchigram [16] and the residual 2-fold astigmatism was corrected using the Z-contrast image. An annular dark-field (ADF) detector (Fischione Model 3000) was used for both Z-contrast and bright-field STEM imaging. Z-contrast images were acquired with a detector inner angle of 65 mrad. The incident probe intensity was measured using the detector preamplifier output voltage with the entire CBED disk placed on a region of the ADF detector known to have a uniform detection efficiency [15]. Bright-field STEM images were acquired with a 2.8 mrad collection aperture semi-angle (the TEM objective aperture)

inserted directly below the sample, as shown schematically in Fig. 1. The pattern was deflected onto the same region of the ADF detector used for the incident probe intensity measurement and the intensity was recorded as the probe was scanned.

For measurements of the local sample thickness, PACBED patterns [3, 17] were acquired with a Gatan Ultrascan 1000 charge-coupled device (CCD) camera by scanning the probe at each image location. Fine details in the PACBED patterns change rapidly with thickness, allowing for accurate thickness determination within ± 1nm by comparison with simulations [3, 17].

The defocus step size was found using diffractograms of a bright-field STEM defocus series of amorphous $SrTiO_3$, after reducing the noise by using the radial average. The spatial frequency of the maximum in the diffractograms was compared with calculations of the contrast transfer function (CTF) as a function of defocus for the electron optical parameters used here, using the ctemtf MATLAB program in ref. [18]. The comparisons showed that the true defocus step size was a factor of four smaller than the values given by the microscope software. The defocus values were estimated by using the maximum image contrast as a reference value and the calibrated step size. Simulations established that the maximum image contrast was around -70 nm.

The standard deviation of the image intensities, σ, is a measure of image contrast if noise levels are low. Fourier filtering with a low-pass aperture function was used to remove scan and counting statistics noise. To determine the appropriate aperture size that resulted in a correct measure of contrast for the experimental noise level, Gaussian noise was applied with a range of standard deviations to simulated images that were then Fourier filtered. For a

range of noise levels, a low pass aperture radius of 8.9 nm^{-1} resulted in the minimum deviation in the contrast relative to that of simulations without noise. This aperture was applied to filter the experimental images from which contrast values were subsequently determined.

Z-contrast images are dominated by thermally scattered electrons, which must therefore be included in simulations [2, 19, 20]. For quantitative Z-contrast imaging of thicker samples it has been well established that multiple TDS scattering must be taken into account (see, for instance, Ref. [2]). This may be accomplished via the frozen phonon model [18]. However the frozen phonon model is computationally very demanding and bright-field STEM images are expected to be dominated by elastically scattered electrons. To test this, bright-field STEM image simulations were carried out at strategic points in the parameter space relevant to our experimental images comparing the frozen phonon model with the absorptive multislice method. The absorptive multislice method fully accounts for elastic scattering, but only incorporates the effects of thermal scattering through an attenuation of the elastic intensity using an absorptive potential based on the Einstein model [19], i.e. the positive contribution of thermally scattered electrons to the images is not included.

All calculations used a supercell of 13×13 unit cells, on a mesh of 1024×1024 pixels. The frozen phonon model calculations were done on a finer mesh of 2048×2048 pixels to make sure that the sharp atomic potentials that occur in that model were adequately sampled. In all cases we found near perfect agreement, as expected for the relatively small thicknesses used in this experiment. For example, for a thickness of 25 nm and a defocus of -100 nm the mean value of the images calculated are 0.058 for the multislice calculation and 0.061 for the

frozen phonon calculation, while the standard deviations are 0.0265 and 0.0267 respectively. The average of the difference in contrast predicted by the two models was 0.1%, which is significantly less than the experimental error. The close agreement between the two methods demonstrated that including TDS scattered electrons in the images does not significantly affect the contrast for thin specimens in HRTEM/bright-field STEM.

III. Results and Discussion

Experimental bright-field STEM images of a $SrTiO_3$ single crystal are shown in the left columns of Fig. 2 for a range of thickness and defocus values. Contrast reversals and changes in the pattern occur dependent on defocus and thickness, characteristic for coherent interference (phase contrast) images [1, 12]. The labels on each image state its measured contrast value, defined here as the ratio of the standard deviation of the image intensities to the mean image intensity.

Results from calculations using the multislice absorptive model are shown in the right columns in Fig. 2. Spatial incoherence is the combined effect of a finite illumination source size, instabilities, sample drift, etc. [18]. It is taken into account by convolving [2, 21] the simulated images with an effective source distribution function with a full-width at half-maximum (FWHM) of 0.11 nm. Because spatial incoherence is difficult to measure directly in non-aberration corrected STEM [22] several control experiments were performed to ensure the effective source size used here provides a realistic estimate for the spatial incoherence in STEM with this instrument. In particular, the bottom row in Fig. 2 shows Z-contrast images and comparisons with frozen phonon simulations accounting for spatial incoherence. The Z-contrast images were recorded at the same locations as the bright-field

STEM images. A function with a FWHM of 0.11 nm yielded perfect agreement between simulation and experiment in *both* Z-contrast imaging (see bottom row in Fig. 2) *and* in bright-field STEM (as discussed below). The function is thus independent of the scattering processes, which are very different in bright-field STEM and Z-contrast imaging, consistent with the influence of spatial incoherence. The function is furthermore independent of the material and sample thickness, as has been shown previously using materials with a wide range of different scattering cross-sections [3], and thus it is *not* caused by a scattering mechanism not accounted for in the simulations. Furthermore, the *mean* image intensities, which are independent of spatial incoherence, agree quantitatively in both experiments and simulations in both bright-field STEM and Z-contrast imaging (see Fig. 3). Discrepancy in the mean intensities would indicate a redistribution of intensities by a scattering process not accounted for in the simulations, which is clearly not the case.

Figure 2 shows near perfect agreement between simulations and experiments across the entire range of thickness and defocus values. The average contrast mismatch factor between experimental and simulated bright-field STEM images is 1.15. This small residual mismatch is entirely within the experimental uncertainty caused by the noise of the detector, residual astigmatism, drift and, most importantly, the thickness determination (±1 nm). This can be seen more clearly from Fig. 4, which, using the thickness dataset with the largest discrepancy as an example, compares the experimental contrast with simulations with a thickness difference of 1 nm over a wide defocus range. Thus the agreement between experiments and simulations in the bright-field STEM images in this study is within the experimental accuracy. The agreement is independent of defocus and thickness, showing that inelastic scattering does not play a significant role in any residual mismatch.

The results also have implications for conventional HRTEM imaging, where a large mismatch of two to five has been reported [4, 5, 7, 8]. By the principle of reciprocity [1, 12], a pixel in a HRTEM image is equivalent to a pixel in the STEM image collected with a point STEM bright-field detector. Strictly, reciprocity is only exact for elastic scattering. But for high energy electrons it has been shown be an excellent approximation for both thermal scattering [23] and higher energy losses [20]. Therefore the contrast in bright-field STEM images is based on essentially the same electron-specimen interactions as would be present in the reciprocity-related HRTEM experiment. The results thus show that the contrast mismatch in conventional HRTEM is unlikely to be due to an inadequately understood aspect of the electron-specimen interactions. Though the detector size (aperture) used here is larger than the ideal point source, the transition to a point is a well-defined limit [1]. In particular, an HRTEM experiment with an incoherent angular spread in the incident beam equal to the detector collection angle used here is the conjugate by reciprocity of the STEM experiment carried out here. The choice of detector size (aperture) therefore does not affect the conclusions about the scattering physics.

IV. Conclusions

In summary, we have demonstrated excellent agreement between simulation and experiment in bright-field STEM. The excellent agreement in this and in prior studies of Z-contrast images [2, 3] shows that current models of image formation adequately model both low and high-angle scattering, including thermal diffuse scattering. Other inelastic scattering processes do not play a significant role in contrast formation for samples that are sufficiently

thin. Furthermore, inelastic scattering, which by reciprocity is present in bright-field STEM as much as it would be in HRTEM, is not the origin of the contrast mismatch observed in the HRTEM literature for similar specimen thicknesses. Thus the results add to the growing body of evidence that the magnitude of the parallel detector point spread function has been underestimated in prior HRTEM experiments [10].

Acknowledgements

The research at UCSB was supported by the U.S. National Science Foundation (grant number DMR-0804631) and the Department of Energy (DE-FG02-06ER45994). J.M.L. also thanks the U.S. Department of Education for a fellowship under the GAANN program (grant number P200A07044) and the NSF-funded UCSB ICMR (DMR-0409848) for a travel grant to Melbourne to work with L.J.A. The work made use of the UCSB MRL Central facilities supported by the MRSEC Program of the National Science Foundation under award No. DMR 0520415. L.J.A. acknowledges support by the Australian Research Council. S.D.F. is supported as a Japan Society for the Promotion of Science (JSPS) fellow.

References

[1] J. C. H. Spence, *High-Resolution Electron Microscopy* (Oxford Science Publications, 2003).

[2] J. M. LeBeau, S. D. Findlay, L. J. Allen, and S. Stemmer, Phys. Rev. Lett. **100**, 206101 (2008).

[3] J. M. LeBeau, S. D. Findlay, X. Wang, A. J. Jacobson, L. J. Allen, and S. Stemmer, Phys. Rev. B **79**, 214110 (2009).

[4] M. J. Hytch, and W. M. Stobbs, Ultramicroscopy **53**, 191 (1994).

[5] A. Howie, Ultramicroscopy **98**, 73 (2004).

[6] K. A. Mkhoyan, S. E. Maccagnano-Zacher, M. G. Thomas, and J. Silcox, Phys. Rev. Lett. **100**, 025503 (2008).

[7] C. B. Boothroyd, J. Microsc. **190**, 99 (1998).

[8] K. Du, K. von Hochmeister, and F. Phillipp, Ultramicroscopy **107**, 281 (2007).

[9] R. R. Meyer, and A. I. Kirkland, Microsc. Res. Tech. **49**, 269 (2000).

[10] A. Thust, Phys. Rev. Lett. **102**, 220801 (2009).

[11] J. C. H. Spence, and J. M. Cowley, Optik **50**, 120 (1978).

[12] J. M. Cowley, Appl. Phys. Lett. **15**, 58 (1969).

[13] C. L. Jia, and K. Urban, Science **303**, 2001 (2004).

[14] M. Varela, A. R. Lupini, K. van Benthem, A. Y. Borisevich, M. F. Chisholm, N. Shibata, E. Abe, and S. J. Pennycook, Ann. Rev. Mater. Res. **35**, 539 (2005).

[15] J. M. LeBeau, and S. Stemmer, Ultramicroscopy **108**, 1653 (2008).

[16] J. M. Cowley, Ultramicroscopy **4**, 413 (1979).

[17] J. M. LeBeau, S. D. Findlay, L. J. Allen, and S. Stemmer, accepted in: Ultramicroscopy (http://dx.doi.org/10.1016/j.ultramic.2009.10.001).

[18] E. J. Kirkland, *Advanced Computing in Electron Microscopy* (Plenum Press, New York, 1998).

[19] L. J. Allen, S. D. Findlay, M. P. Oxley, and C. J. Rossouw, Ultramicroscopy **96**, 47 (2003).

[20] D. O. Klenov, S. D. Findlay, L. J. Allen, and S. Stemmer, Phys. Rev. B **76**, 014111 (2007).

[21] P. D. Nellist, and J. M. Rodenburg, Ultramicroscopy **54**, 61 (1994).

[22] C. Dwyer, R. Erni, and J. Etheridge, Appl. Phys. Lett. **93**, 021115 (2008).

[23] A. P. Pogany, and P. S. Turner, Acta Cryst. A **24**, 103 (1968).

Figure captions

Figure 1 (color online):

Schematic showing image formation in bright-field STEM using a TEM/STEM instrument: a focused coherent probe is scanned across the specimen and electrons are collected with a small aperture detector (ideally a point) in the forward direction. The ray diagram (green cone) is drawn to illustrate the collection angle in STEM. The TEM objective aperture (below the specimen) was used to limit the detector collection angle. Electrons that passed through the aperture were deflected onto the ADF detector and serially collected by scanning the incident probe.

Figure 2 (color online):

Top rows: experimental bright-field STEM images (left panel in each column, unfiltered) compared to multislice absorptive model calculations (right panel in each column). The upper labels in each image show their contrast values. The lower (black background) labels state the defocus, with underfocus being negative. Bottom row: experimental and simulated Z-contrast images (54 nm underfocus). Note that all images are on an absolute intensity scale relative to the incident probe and reported as a fraction of the incident probe intensity. For the Z-contrast images, the experimental contrast value at a thickness of 4 nm suffers from the image intensities being in the level of the noise and is not provided. The simulations have been convolved with a Gaussian of 0.11 nm FWHM to account for the effects of a finite source size.

Figure 3 (color online):

Comparison of the mean intensities in simulation and experiment for (a) bright-field STEM and (b) Z-contrast STEM images. Note that all images are on an absolute intensity scale relative to the incident probe and reported as a fraction of the incident probe intensity. The horizontal error bars are ± 1 nm, corresponding to the uncertainty in the thickness determination. Excellent agreement is achieved within the ± 10% vertical error bars that are provided as a visual aid.

Figure 4 (color online):

Contrast in bright-field STEM images as a function of defocus for region of the sample with thicknesses of ~ 14 nm (experiment) and 14 and 15 nm (simulations). As a visual aid, error bars of ±10% are shown for the experiments. The grey shaded region indicates a range of contrast values that lies between those calculated for the 14 and 15 nm thick samples.

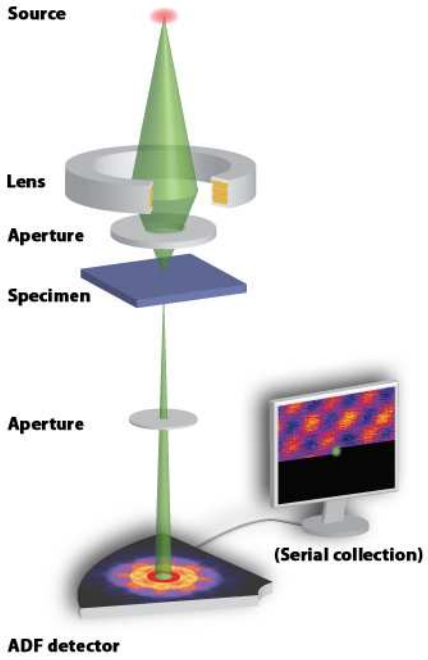

Figure 1 BJ11212 14OCT2009

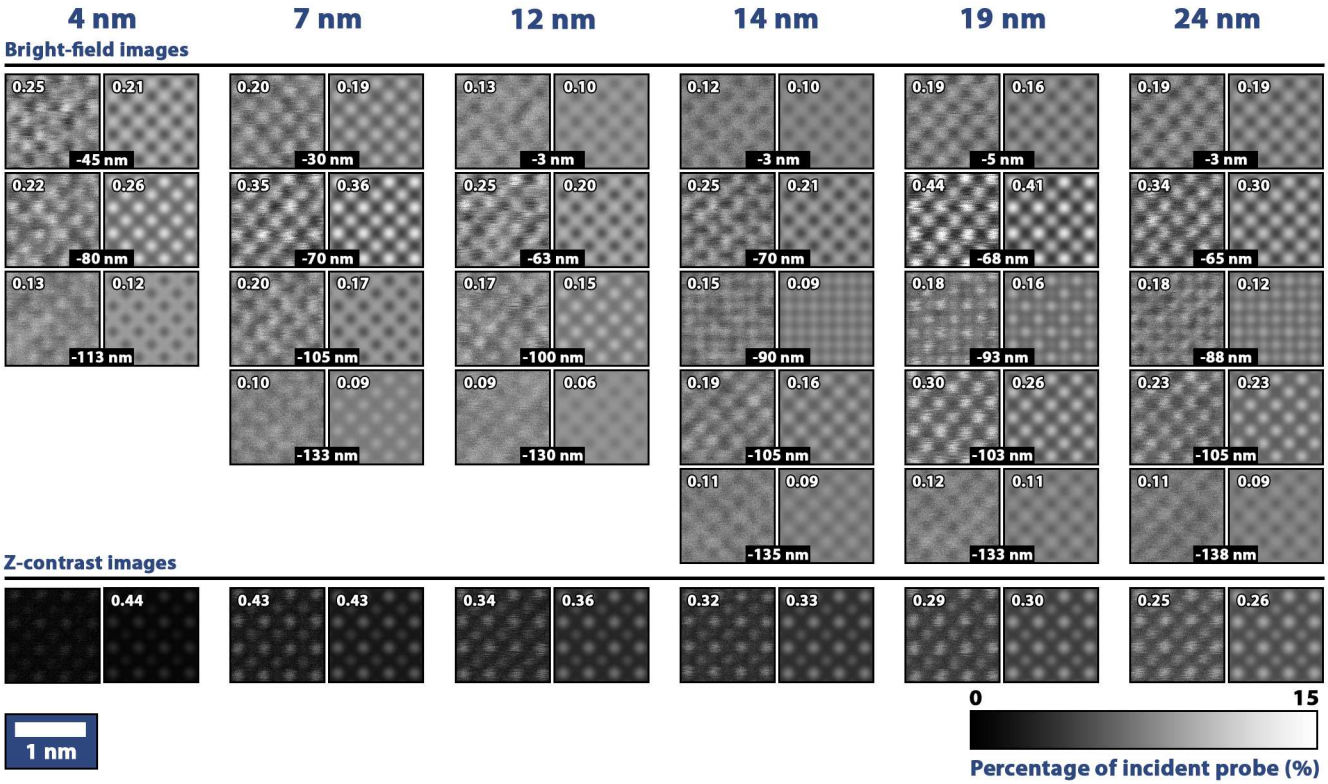

Figure 2 BJ11212 14OCT2009

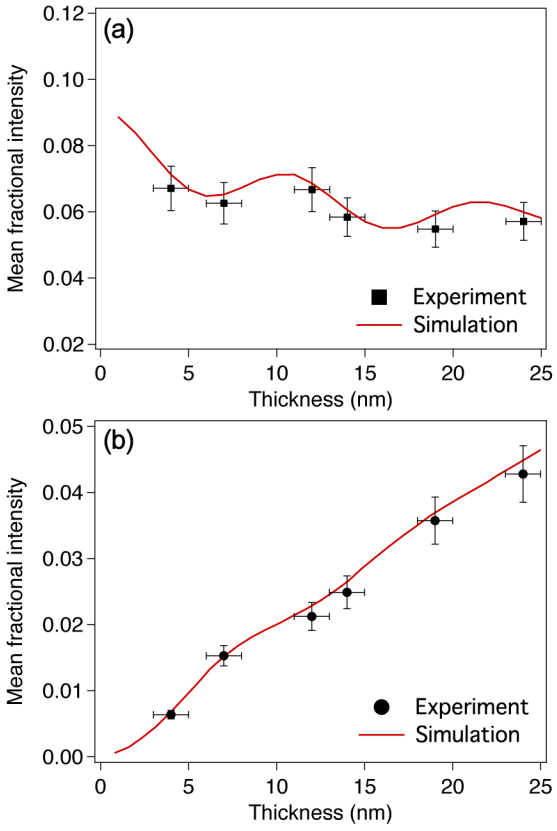

Figure 3 BJ11212 14OCT2009

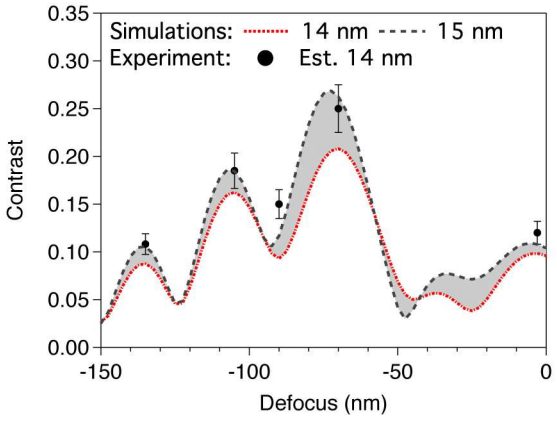

Figure 4 BJ11212 14OCT2009